Decoupled Ion Transport via Triadic Molecular Synergy in Flame-Retardant Quasi-Solid Electrolytes for Safe Lithium-Metal Batteries

Kun Li, Anjun Hu, Ruizhe Xu, Wang Xu, Borui Yang, Ting Li, Yuanjian Li, Zhi Wei Seh, Jianping Long*, Shimou Chen**

K. Li, Dr. A. Hu, R. Xu, W. Xu, B. Yang, T. Li, Prof. Dr. J. Long
College of Materials and Chemistry & Chemical Engineering (College of Lithium Resources and Lithium Battery Industry), Chengdu University of Technology, Chengdu 610059, China
E-mail: anjunhu@cdut.edu.cn; longjianping@cdut.cn

Prof. Dr. S. Chen
State Key Laboratory of Chemical Resource Engineering, Beijing Key Laboratory of Electrochemical Process and Technology of Materials, Beijing University of Chemical Technology, Beijing 10029, P. R. China
E-mail: chensm@buct.edu.cn

Dr. Y. Li, Prof. Dr. Z. Seh
Institute of Materials Research and Engineering (IMRE), Agency for Science, Technology and Research (A*STAR) 2 Fusionopolis Way, Innovis #08-03, Singapore 138634, Republic of Singapore

Dr. A. Hu
Lithium Resources and Lithium Materials Key Laboratory of Sichuan Province, Chengdu 610059, Sichuan, China

Abstract

Ionic liquids (IL)-based quasi-solid polymer electrolytes (QSPEs) hold promise for safe lithium metal batteries owing to their tunable electrochemical properties and processability. However, traditional design strategy has ignored the interdependencies among "component-function-interface", leading to compromised practical applications hindered by sluggish lithium-ion transport kinetics and safety concerns. Herein, we propose a triadic molecular synergy paradigm to decouple lithium-ion conduction mechanisms in flame-retardant QSPEs. Pentaerythritol tetraacrylate-LiTFSI provides the structural framework, while the IL (1-butyl-3-methylimidazole bis (trifluoromethylsulfonyl) imide, BmimTFSI) as a plasticizer softens the polymer chains by weakening the intermolecular forces to provide an additional ion-transport pathway while imparting flame-retardant properties. Additionally, the highly electronegative fluorine atoms of the additive (2-(perfluorohexyl)ethyl methacrylate, PFMA) promote LiTFSI dissociation through electron cloud migration, simultaneously immobilizing $TFSI^-$ anions and suppressing cationic competition through strong PFMA−$Bmim^+$ coordination. As a proof-of-concept, this synergistic design achieves a high lithium-ion transference number (0.72), forms a stable lithium fluoride-dominated interphases, and enhances battery safety via a condensed-phase flame-retardant mechanism. Experimental validation demonstrates that the designed quasi-solid electrolyte significantly enhances cycling stability in Li symmetric cells, Li||$LiFePO_4$ and Li||$LiNi_{0.8}Co_{0.1}Mn_{0.1}O_2$ cells. The proposed molecular engineering strategy establishes a paradigm for developing high-performance QSPEs in lithium metal batteries.

1. Introduction

Solid-state lithium metal batteries (SSLMBs) are hailed as the most promising next-generation energy storage systems owing to their ultrahigh energy density and intrinsic safety.[1] The commercialization of SSLMBs critically relies on the advancement of solid-state electrolytes.[2] Among various candidates, solid polymer electrolytes (SPEs) are favored for practical applications due to their mechanical properties and interface contact.[3] Nevertheless, the practical implementation of SPEs faces challenges. The high crystallinity of SPEs significantly limits their room-temperature ionic conductivity (10^{-7}~10^{-4} S cm^{-1})[4], thereby hindering its practical applications. Moreover, SPEs are prone to decomposition and combustion under thermal abuse conditions, posing a potential risk of thermal runaway.[5] Therefore, it is challenge to achieve both fast ion conduction and high safety of traditional SPEs.[6]

While strategies like polar side-chain functionalization[7] and amorphous-phase engineering[8] can moderately enhance ionic transport, these single-component modifications often struggles to simultaneously meet the requirements of rapid ionic conduction and flame retardancy. In contrast, the conversion of a solid polymer electrolyte to a quasi-solid polymer electrolyte (QSPEs) using a non-combustible ionic liquid (IL) plasticizer can be a straightforward and compromising strategy to improve ion conductivity (>10^{-4} S cm^{-1}) by reducing the crystallinity of the polymer and introducing additional pathways for ion transport.[9] However, the high viscosity and large competing cations of ionic liquids greatly hinder the transport of metal ions. Therefore, the key to achieving safe and fast ion conduction in IL-based quasi-solid polymer electrolytes hinges on migrating the negative effects of each component.[10]

In recent years, despite considerable efforts to decouple ionic transport through binary strategies (e.g., polymer-IL composites), fundamental limitations persist in QSPEs.[11] Specifically, while IL plasticizers effectively suppress polymer crystallization, the concomitant competitive migration between Li^+ and large cations ($EMIM^+$) depresses ionic conductivity. On the other hand, although the introduction of flame-retardant components improves the thermal stability, their decomposition

products will significantly degrade the interfacial stability.[12] In addition, the high viscosity of IL causes the double layer reconstruction effect at the electrode interface, which makes the interface charge transfer impedance surge. This triple interlocking effect of composition-function-interface makes the cooperative optimization of fast ion transport and intrinsic safety a scientific barrier in the development of QSPEs.

Herein, we propose a molecular-level triadic synergy strategy that integrates the advantages of polymer-salt, IL, and fluorinated copolymer additives (**Figure 1**). Pentaerythritol tetraacrylate (PETEA) combined with lithium bis(trifluoromethanesulfonyl)imide (LiTFSI) forms the structural framework. The 1-Butyl-3-methylimidazolium bis(trifluoromethylsulfonyl)imide (BmimTFSI) was introduced as a dynamic plasticizer to reduce crystallinity by weakening the interchain forces of the polymer while providing flame retardancy. In addition, a fluorinated copolymer additive, 2-(perfluorohexyl)ethyl methacrylate (PFMA), was incorporated to reduce the viscosity of BmimTFSI and initiate cross-linking reactions with PETEA. As elucidated through theoretical calculations and experiments, the highly electronegative fluorine atoms of PFMA promote LiTFSI dissociation by electron cloud migration. At the same time, the electronegative fluorine sites inhibit $TFSI^-$ anion migration, enhancing Li^+ conductivity. Finally, the strong binding between large $Bmim^+$ cations and PFMA suppresses cation competition, significantly improving Li^+ conduction. The synergy among components endows the electrolyte with high ionic conductivity (1.84×10^{-3} S cm^{-1}) and an elevated Li^+ transference number (0.72) at 25 °C. As a result, this quasi-solid electrolyte demonstrates exceptional plating/stripping cycling stability, exceeding 3500 hours in Li symmetric cells. In addition, the Li||$LiFePO_4$ (LFP) cell retains 80% of its initial capacity over 600 cycles and the Li||$LiNi_{0.8}Co_{0.1}Mn_{0.1}O_2$ (NCM811) cell maintains 80% of its initial capacity over 240 cycles. Importantly, BmimTFSI promotes the formation of an intact carbon layer during combustion, reducing heat release through a condensed-phase flame-retardant mechanism. This work breaks the boundary of electrolyte performance through triadic synergy mechanism, providing a new paradigm for the development of LMBs.

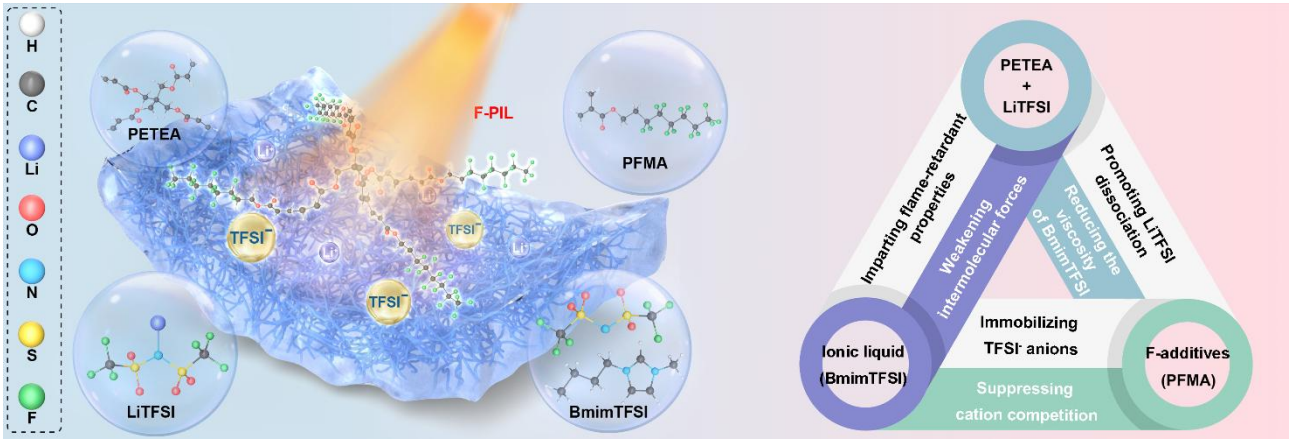

Figure 1. Schematic diagram of molecular-level triadic synergy strategy for F-PIL.

2. Results and Discussion

2.1. Construction and properties of F-PIL

Fluorinated polymer-encapsulated ionic liquid quasi-solid electrolytes (F-PIL) were prepared by *in-situ* polymerization. The polymer salt (PS) system was composed of PETEA and LiTFSI as the host matrix. By introducing PFMA as the functional side chain and BmimTFSI as the plasticizer, the F-PIL electrolyte system was successfully synthesized. The structural design of F-PIL is presented in **Figure 2**a. Fourier-transform infrared (FTIR) spectroscopy spectral analysis indicates that F-PIL did not present a stretching vibration peak at 1630 cm^{-1} (Figure 2b), confirming the successful synthesis of the polymer. Macroscopically, F-PIL presents a non-flowing solid state (Figure S1). To optimize the performance of F-PIL, the influence of different component ratios on the conductivity was systematically investigated. Conductivity measurements at different temperatures (Figure 2c and Figure S2) reveals that the system exhibits the highest ionic conductivity when the LiTFSI concentration was 0.5 M and the PFMA mass fraction is 5 wt%. The specific values are shown in Figure 2d. At room temperature, the ionic conductivity of F-PIL reached 1.84 mS cm^{-1}. The lithium-ion transference number (t_{Li}^{+}) in the F-PIL system is 0.72, significantly higher than that of traditional PIL (Figures 2e, S3, and S4), indicating a higher degree of Li^{+} dissociation and enhanced dynamic coordination stability with its carbonyl groups. To offer a comprehensive comparison of the ionic conductivity, t_{Li}^{+}, and Li^{+} conductivity of the F-PIL electrolyte with those of other polymer electrolytes, we have summarized the data in a three-dimensional radar chart (Figure 2f and Table S1). This analysis underscores the superior Li^{+} conductivity of the F-PIL electrolyte.[13]

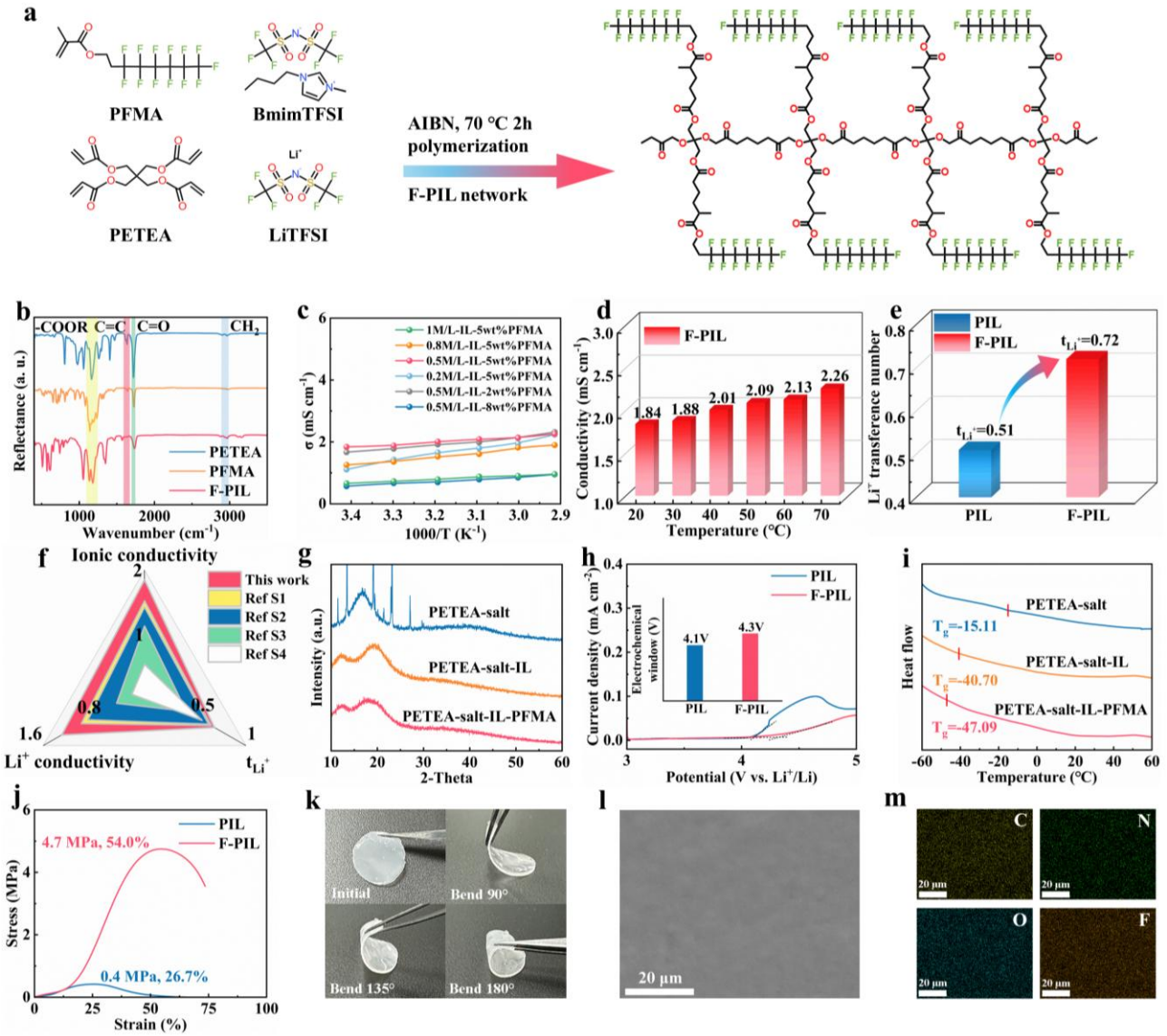

Figure 2. Synthesis and properties of F-PIL. (a) Schematic diagram of F-PIL. (b) FTIR spectra of PETEA, PFMA and F-PIL. (c) Temperature dependence of ionic conductivity for different ratios of F-PIL. (d) Comparison of ionic conductivity with temperature of F-PIL. (e) t_{Li^+} of F-PIL and PIL. (f) Comparison of ionic conductivity, t_{Li^+} value and Li^+ conductivity (ionic conductivity * t_{Li^+} value) between F-PIL and other polymeric IL electrolytes. (g) XRD patterns of PETEA-salt, PETEA-salt-IL, and PETEA-salt-IL-PFMA. (h) Linear sweep voltammetry curves for F-PIL and PIL. (i) DSC curves of PETEA-salt, PETEA-salt-IL, and PETEA-salt-IL-PFMA. (j) Stress-strain curves of F-PIL and PIL. (k) mechanical properties of F-PIL. (l) Top-view SEM image of the F-PIL and (m) corresponding EDS element mapping.

Before the addition of the IL, the PS system exhibited high crystallinity, as evidenced by distinct X-ray diffraction (XRD) peaks corresponding to the crystalline regions of polymer and undissolved salts. The introduction of BmimTFSI induces a quasi-solid state, characterized by a prominent amorphous region in the XRD pattern. This change is attributed to IL and increased salt dissolution, which softens the polymer chain. The incorporation of PFMA further reduces the crystallinity of F-PIL (Figure 2g). Additionally, the high bond energy of the C−F bond in PFMA provides enhanced

oxidative stability (4.3 V) for F-PIL compared to that of PIL (4.1 V) (Figure 2h). The glass transition temperature (Tg) was determined via differential scanning calorimeter (DSC) test. The weakening of intermolecular forces by BmimTFSI reduces the Tg of F-PIL to −47.09 ℃ (Figure 2i). The stress-strain curve reveals superior fracture strength (4.7 MPa) and elongation (54.0%) for F-PIL compared to PIL (0.4 MPa, 26.7%) (Figure 2j). The excellent flexibility of F-PIL enables remarkable mechanical properties without cracking or fractures during the bending process (Figure 2k). Scanning electron microscopy (SEM) (Figure 2l) and energy-dispersive X-ray spectroscopy (EDS) mapping (Figure 2m) further confirms the tightness and uniformity of F-PIL.

2.2. Thermal stability of F-PIL

Thermogravimetric (TG) analysis was conducted to assess the thermal stability of the F-PIL and PS system (Figure S5). The C−F bond exhibits a high bond dissociation energy, contributing to the stability of the C−F bond during heating, making it less prone to breaking. As a result, the thermal decomposition temperature of F-PIL (340 °C) is higher than that of PIL (321 °C). F-PIL demonstrates excellent flame retardancy, attributed to the incorporation of the non-combustible BmimTFSI. When exposed to a flame, F-PIL does not ignite within 10 seconds, indicating its potential to mitigate fire risks caused by battery short circuits and enhance the safety of LMBs (**Figure 3**a). Figure 3b schematically speculates the flame-retardant mechanism of F-PIL. The three-dimensional network structure of F-PIL enhances its carbonization capability during combustion. This structural promotes a continuous residual carbon phase, ensuring uniform carbonization layer formation. The physical barrier effect of F-PIL prevents direct flame-material contact, suppressing heat transfer and flame propagation. Consequently, F-PIL demonstrates superior thermal stability and flame-retardant performance.

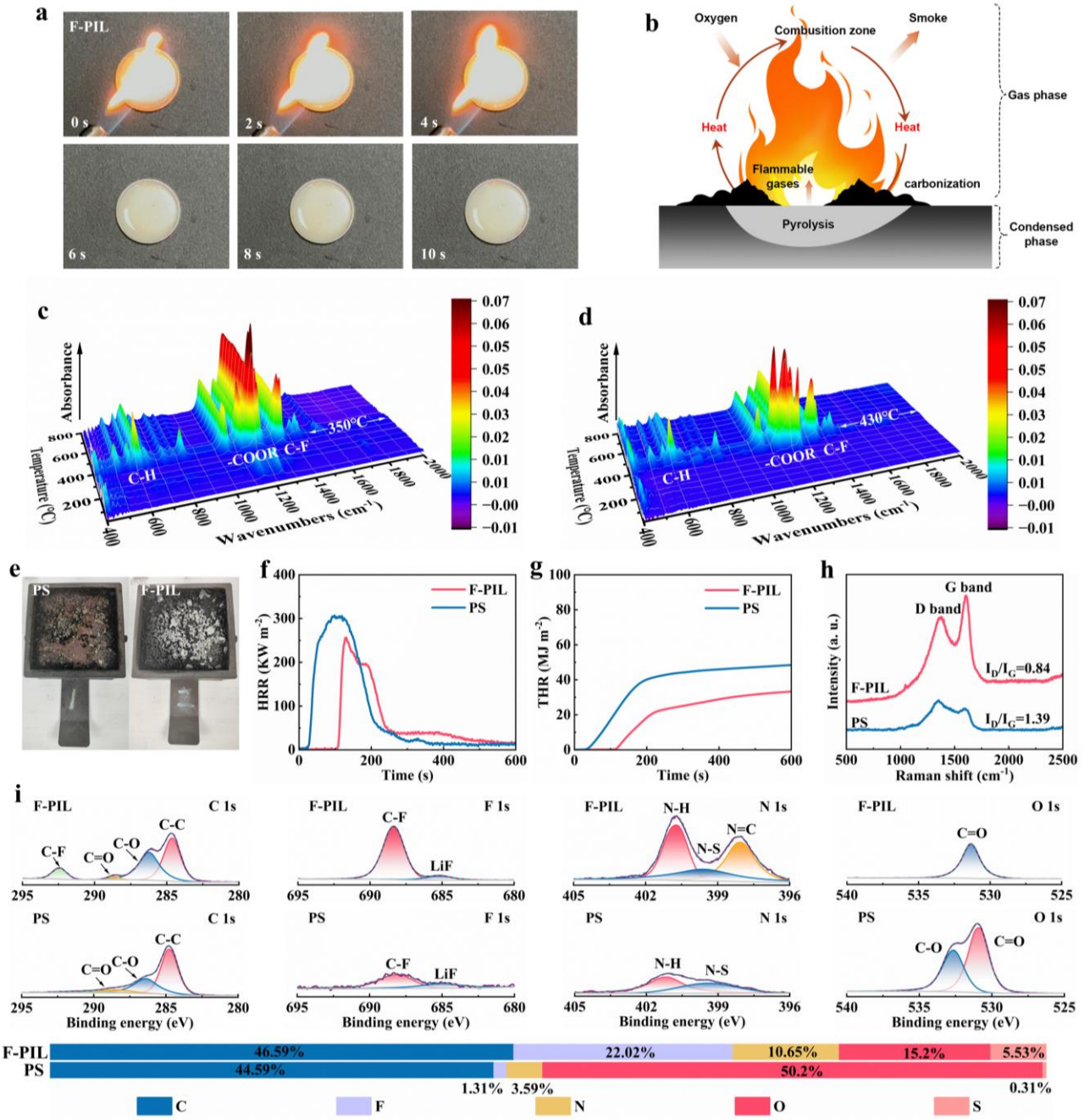

Figure 3. Flame retardancy evaluation of F-PIL. (a) Combustion test of F-PIL. (b) Flame-retardant mechanism of flame retardancy of F-PIL. 3D TG-FTIR spectrum of the gases from thermal treatment of (c) PS and (d) F-PIL heated at 10 °C min^{-1}. (e) Digital photographs of residual carbon layers for PS and F-PIL after combustion. (f) HRR and (g) THR of PS and F-PIL. (h) Raman spectra of the char residue of PS and F-PIL. (i) XPS spectra of char residue for PS and F-PIL.

To this end, a series of characterizations were used to study the pyrolysis products and verify the combustion mechanism. TG-FTIR analysis identifies the characteristics of gas-phase products during pyrolysis. The absorption peak of the −COOR in PS appears at 1000-1300 cm^{-1} around 350 °C (Figure 3c), a region typically associated with high flammability in polymers after volatilization. In contrast, for F-PIL, the absorption peak of −COOR shifts to around 430 °C with significantly reduced

intensity (Figure 3d), indicating the influence of BmimTFSI and PFMA in suppressing polymer decomposition and reducing flammability.[14] After cone calorimeter testing, the uniform and intact carbon residue observed on the surface of the F-PIL surface (Figure 3e) suggests the formation of long carbon chains promoted by the introduction of BmimTFSI and PFMA, This contributes to the formation of a homogeneous and continuous carbon layer, which imparts condensed-phase flame retardancy. Heat release rate (HRR) and total heat release (THR) parameters reveals that F-PIL exhibits superior heat resistance, with an ignition time of approximately 105 seconds compared to that of PS (25 seconds) (Figures 3f and 3g). Additionally, the lower HRR and THR rate of F-PIL compared to PS further emphasize its reduced fire risk. In fire scenarios, smoke and toxic gas emissions pose greater threats than flame and heat. F-PIL's ability to reduce heat release and control flame size and spread significantly decreases total smoke production (Figure S6). Lower CO_2 and CO production rates (Figures S7 and S8) further demonstrate that BmimTFSI and PFMA in F-PIL retard thermal decomposition and more char formation.[15]

the characteristics of char layer were analyzed using Raman and X-ray photoelectron spectroscopy (XPS). Figure 3h reveals characteristic peaks at 1350 cm^{-1} (D band) and 1590 cm^{-1} (G band) for the charred electrolyte. The D-to-G bond intensity ratio (I_D/I_G) reflects the degree of graphitization, with lower ratio indicating a more ordered structure. The I_D/I_G ratio for F-PIL (0.84) is lower than that for PS (1.39), suggesting that F-PIL forms a more regular char layer during combustion.[16] The XPS spectra of the char layer on for both PS and F-PIL were shown in Figures 3i and S9. The XPS spectra confirm that the carbon residue contains primarily C, F, N, and O elements. The C 1s region shows that the layer is mainly composed of C−C, C−O, and C=O bonds, which results from the decomposition of the polymer's −COOR groups. As evidenced by the F 1s region, the presence of increased C−F bonding in F-PIL reflects the incorporation of the fluorine-containing monomer. Additionally, the N 1s spectra show N−H and N−S bonds in both PS and F-PIL from the $TFSI^-$ anion, along with N=C bonds originating from the $Bmim^+$ cation in the IL. The O 1s spectra indicates that the residual carbon in PS predominantly contains C−O and C=O bonds. These findings

demonstrate that both PFMA and BmimTFSI contribute to the formation of char layer during combustion.[17]

2.3. Dissociation behavior and ion transport characteristics

The lithium salt dissociation dynamics and ion transport mechanisms of P-FIL were comprehensively elucidated through multiscale characterization and theory simulations. FTIR reveals a coordination-sensitive S−N stretching vibration of $TFSI^-$ at 740 cm^{-1}, with the cation coordination ratio decreasing from 28.7% in PIL to 20.1% in F-PIL (**Figure 4**a), indicative of enhanced liberation of free $TFSI^-$ species and consequent Li^+ release. Raman spectral deconvolution resolved three dissociation states: free ions (FI) (738 cm^{-1}), loose ion pairs (LIP) (742 cm^{-1}), and tightly bound ion pairs (IIP) (746 cm^{-1}). The IIP content reduction from 30.24% in PIL to 17.58% in F-PIL (Figures 4b and4 c) confirms superior LiTFSI dissociation efficiency, with FI and LIP becoming dominant through weakened Li^+−$TFSI^-$ interactions.[18] ^7Li nuclear magnetic resonance (NMR) spectra corroborates these findings (Figure 4d). The narrowed half-peak width (0.015 ppm of P-FIL *vs.* 0.017 ppm of PIL) reflects reduced Li^+ coordination heterogeneity, while the upfield chemical shift (−1.01 ppm of P-FIL *vs.* −1.03 ppm of PIL) confirms attenuated Li^+−anion electrostatic interactions.[19] Density functional theory (DFT) calculations further reveal a reduced LiTFSI dissociation energy in F-PIL (4.89 eV of P-FIL *vs.* 5.25 eV of PIL; Figure S10), attributed to ion−dipole interactions weakening Li^+−$TFSI^-$ bonds. Differential charge analysis (Figure S11) highlights increased electron transfer from polymer C=O groups to LiTFSI, facilitating dissociation in F-PIL.

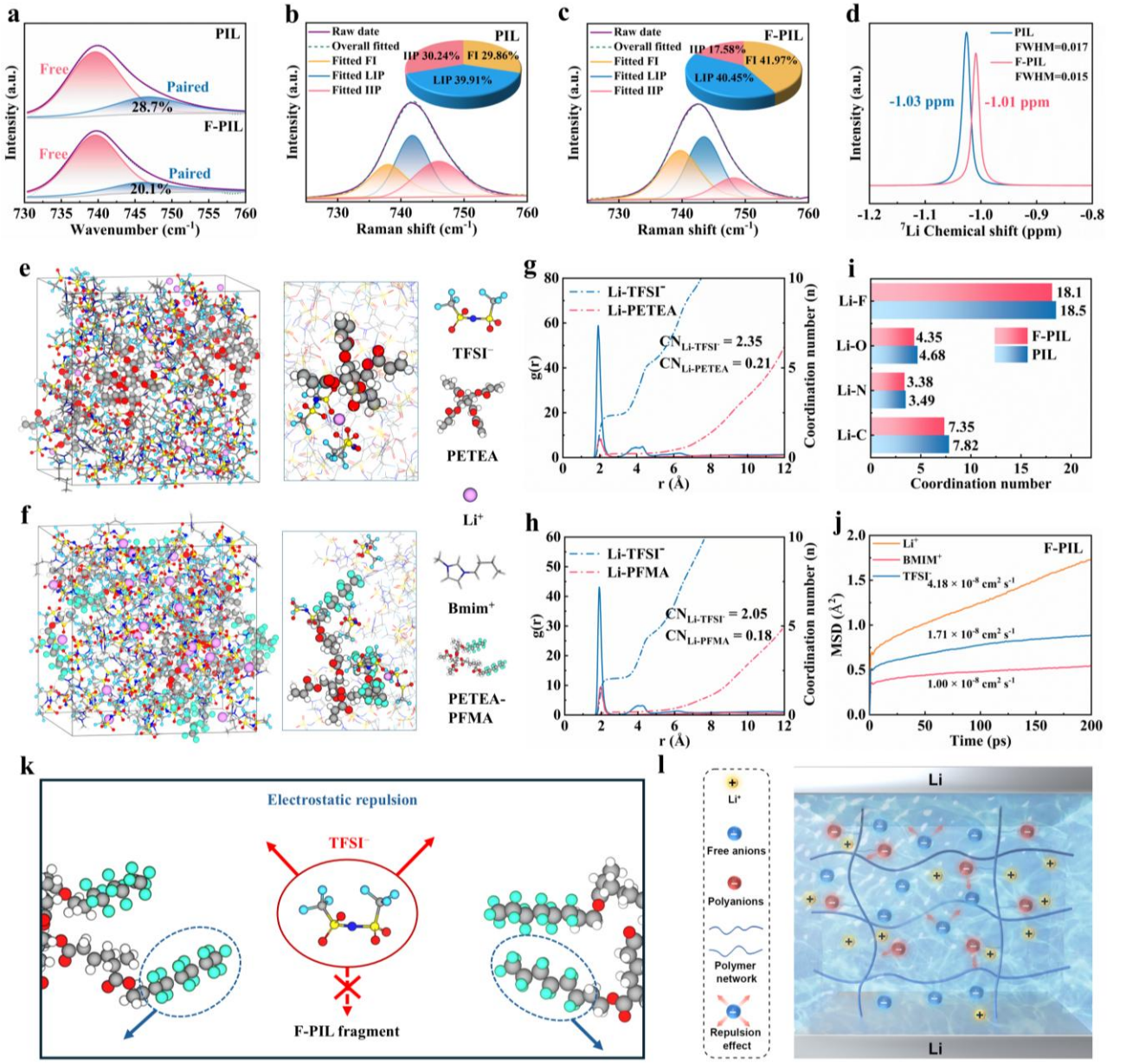

Figure 4. Dissociation behavior and ion transport characteristics. (a) FTIR spectra of PIL and F-PIL. Raman spectra of (b) PIL and (c) F-PIL. (d) ^{7}Li NMR of PIL and F-PIL. (e) MD simulation snapshots of system I (PIL) including PETEA, LiTFSI and BmimTFSI. (f) MD simulation snapshots of system II (F-PIL), addition of PFMA into system I. Radial distribution functions in (g) system I and (h) system II. (i) Coordination number of Li with F, O, N, C atoms in PIL and F-PIL. (j) Mean square displacement and diffusion coefficients of Li^+, $Bmim^+$ and $TFSI^-$ in F-PIL. Schematic of (k) localized and (l) overall anion repulsion in F-PIL.

Molecular dynamics (MD) simulations were used to elucidate the Li^+ coordination environment and transport dynamics in F-PIL and PIL. The MD snapshots (Figures 4e and 4f) reveal a more dispersed Li^+–$TFSI^-$ coordination compared to PIL. Calculated coordination number (CN) demonstrate reduced Li^+–$TFSI^-$ interactions in F-PIL (CN = 2.05) relative to PIL (CN = 2.35) (Figures 4g and 4h), effectively suppressing tight ionic clustering. The CN values of Li^+ with C, N, O, and F atoms in F-PIL are slightly lower than those in PIL (Figure 4i). This reduction is attributed to

the higher dissociation of LiTFSI and the looser coordination environment of Li^+ in F-PIL. Enhanced Li^+ mobility in F-PIL manifests in a 50% higher diffusion coefficient (4.18×10^{-8} cm^2 s^{-1} for F-PIL *vs.* PIL's 2.79×10^{-8} cm^2 s^{-1} for PIL) derived from mean-square displacement analysis (Figures 4j and S12). Furthermore, the Li^+ migration process is influenced by the competitive migration of $Bmim^+$ and $TFSI^-$, where restricting the movement of $TFSI^-$ and $Bmim^+$ reduces the transport barrier for Li^+. In F-PIL, the diffusion coefficients of $Bmim^+$ and $TFSI^-$ are 1.00×10^{-8} cm^2 s^{-1} and 1.71×10^{-8} cm^2 s^{-1}, respectively, both of which are lower than the values for PIL (1.26×10^{-8} cm^2 s^{-1} for $Bmim^+$ and 2.68×10^{-8} cm^2 s^{-1} for $TFSI^-$). DFT-calculated coordination energies (Figure S13) corroborate this trend, with reduced F-PIL−$Bmim^+$ binding energy confirming hindered $Bmim^+$ migration.[20]

Additionally, the F-rich substituents of PFMA on the side chains hinder the transfer of $TFSI^-$ due to the repulsive effect of the electronegative F atoms (Figure 4k). This interaction facilitates the easier migration of Li^+ by restricting $TFSI^-$ movement. Figure 4l schematically illustrates this repulsion mechanism in the F-PIL system, where free anions encounter strong repulsive forces at electronegative sites, reducing their transport rate and overall mobility.[21]

2.4. Interfacial stability of F-PIL and Li metal

The stability of the F-PIL against the Li anode was assessed using half-cell configuration. The cyclic voltammetry (CV) curves of symmetric cells (Figure S14) were analyzed using a Tafel plot to determine exchange current density, revealing that F-PIL exhibits a higher Li^+ transport capability (0.108 mA cm^{-2}) compared to PIL (0.082 mA cm^{-2}) (**Figure 5**a). This superior performance is attributed to the higher intrinsic conductivity of F-PIL, which reduces interface resistance. Moreover, interface impedance, influenced by temperature, was characterized using Nyquist plots across 30−70°C (Figure S15). At all temperatures, F-PIL exhibits lower interface impedance than PIL, demonstrating enhanced interfacial compatibility. The interfacial activation energy (Ea) (Figure 5b) for F-PIL (0.30 eV) is significantly lower than that of PIL (0.39 eV), indicating a reduced Li^+ deposition barrier. Critical current density (CCD) was measured using stepwise constant current

cycling. Starting at 0.1 mA cm^{-2}, Li|F-PIL|Li cell maintains operation until failure at higher currents (0.9 mA cm^{-2}), compared to 0.6 mA cm^{-2} for Li|PIL|Li.

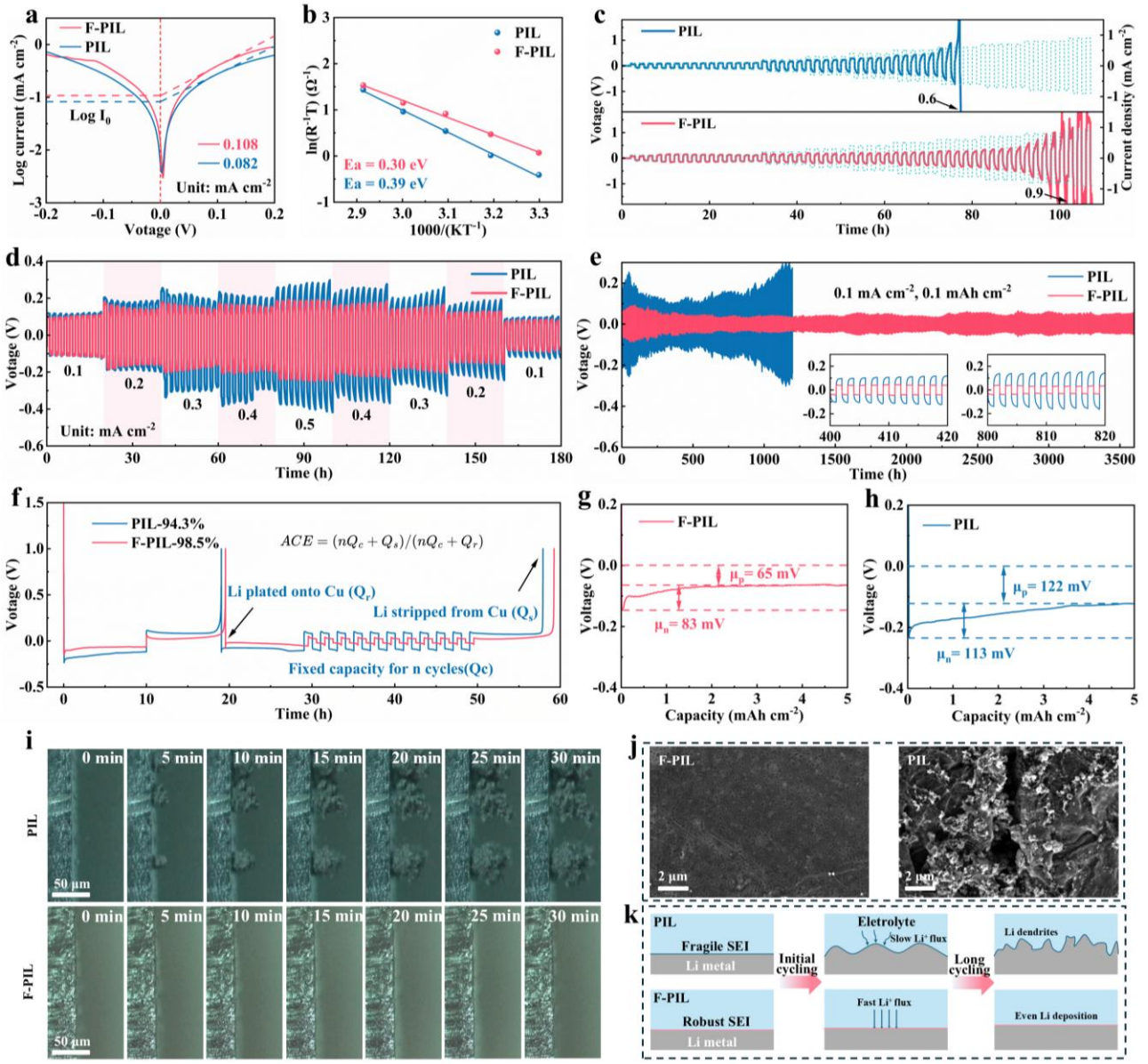

Figure 5. Electrochemical properties and deposition behavior of half-cells. (a) Tafel plots and exchange current density of Li||Li cell using F-PIL and PIL. (b) Arrhenius plots for calculating Ea. (c) CCD measurements of PIL and F-PIL. (d) Rate performance time-voltage curve of Li||Li cell using F-PIL and PIL. (e) Cycling performance time-voltage of Li||Li cell using F-PIL and PIL at 0.1 mA cm^{-2} (inset shows the local time-voltage curve). (f) Time-voltage curve profiles during the average CE test in PIL and F-PIL. Capacity voltage curves of the Li plating process using (g) F-PIL and (h) PIL. (i) Snapshots of the *in-situ* optical microscope observations on the Li anode surfaces in the PIL and F-PIL during plating. (j) SEM images of the cycled lithium anodes with the PIL and F-PIL. (k) Schematic illustration of Li deposition on PIL and F-PIL.

Pating/stripping cycling of symmetric cells were conducted to evaluate the stability of the F-PIL against the Li anode. These cells were cycled at current densities ranging from 0.1 to 0.5 mA cm^{-2}, with 10 cycles at each density (Figure 5d). The Li|F-PIL|Li cell exhibits stable cycling behavior

without significant increase in polarization voltage across all current densities. Upon reverting to 0.1 mA cm^{-2}, the polarization voltage stabilizes again, indicating excellent interfacial stability. In contrast, Li|PIL|Li exhibits significantly higher voltage polarization. Extended plating/stripping experiments at 0.1 mA cm^{-2} further highlights the superior long-term cycling stability of Li|F-PIL|Li, which operates stably for over 3500 hours without short-circuiting, whereas Li|PIL|Li failed after 1200 hours (Figure 5e). The increased polarization voltage observed for PIL is attributed to a high resistance SEI layer formed between PIL and Li metal. Additionally, Li||Cu half-cells were utilized to compare the Li plating/stripping coulombic efficiency (CE). The F-PIL cell demonstrates superior performance, achieving an average CE of 98.5% for partial lithium plating compared to 94.3% for PIL (Figure 5f). To assess the energy barriers for Li^+ nucleation and growth within the SEI layer, the nucleation overpotential (μ_n) and plateau overpotential (μ_p) were calculated. The μ_n (83 mV) and μ_p (65 mV) values for F-PIL (Figure 5g) are lower than those for PIL (Figure 5h), suggesting lower nucleation and growth barriers.[22]

In-situ optical microscopy was employed to monitor the effect of the electrolyte on Li deposition in Li|PIL|Li and Li|F-PIL|Li symmetric cells. Optical microscopy captured real-time images every 5 minutes (Figure 5i), revealing that mossy lithium formed on the Li|PIL|Li surface within 10 minutes, with dendrite formation becoming extensive within 30 minutes. In comparison, Li|F-PIL|Li exhibits uniform lithium plating with dendrite free formation. SEM images after 50 cycles confirmed these observations, showing a more homogeneous and dense lithium deposition morphology on the Li|F-PIL|Li cells (Figure 5j). The surface evolution processes of Li metal anodes in PIL and F-PIL electrolytes were compared in Figure 5k. The PIL electrolyte reacts with lithium to form a chemically unstable SEI with structural defects, leading to uneven Li^+ distribution and Li dendritic growth during cycling. In contrast, the F-PIL electrolyte facilitates the formation of a mechanically stable SEI that can accommodate volume changes in the lithium anode. Moreover, the F-PIL electrolyte exhibits higher ionic conductivity and Li^+ transference number, ensuring both uniform Li^+ flux and fast ion

transport at the electrode interface. These features collectively promote compact lithium deposition and effectively suppress dendrite formation.

2.5 Morphology and composition of electrode/electrolyte interface

To investigate the interfacial composition, the highest occupied molecular orbital (HOMO) and the lowest unoccupied molecular orbital (LUMO) energy levels were calculated to evaluate the redox activity (**Figure 6**a).[23] PFMA exhibits a lower LUMO (−2.55 eV), indicating that PFMA can readily accept electrons, facilitating the cleavage of C−F bond and increasing the concentration of free F^- ions in the electrolyte. These F^- ions react with Li^+ at the electrode interface to form LiF, contributing to the formation of LiF-rich SEI and cathode electrolyte interphase (CEI). The composition of the CEI in both F-PIL and PIL was analyzed using XPS. The decomposition of C−F bonds in PFMA is evident from the reduced C−F peaks in the C 1s spectra (Figure S16a). The CEI in F-PIL (Figure S16b) contains a higher percentage of LiF compared to the CEI in PIL (Figure S17b). Atomic force microscopy (AFM) provides the morphology and mechanical properties of the CEI (Figures 6b and 6c). The CEI of F-PIL exhibits a Young's modulus of 1925 MPa and a smooth surface, while the CEI in PIL shows a lower Young's modulus of 328 MPa and higher roughness (329 nm). The 3D visualization insets further confirm that the CEI in F-PIL has a more planar morphology, supporting its superior mechanical stability and uniformity.

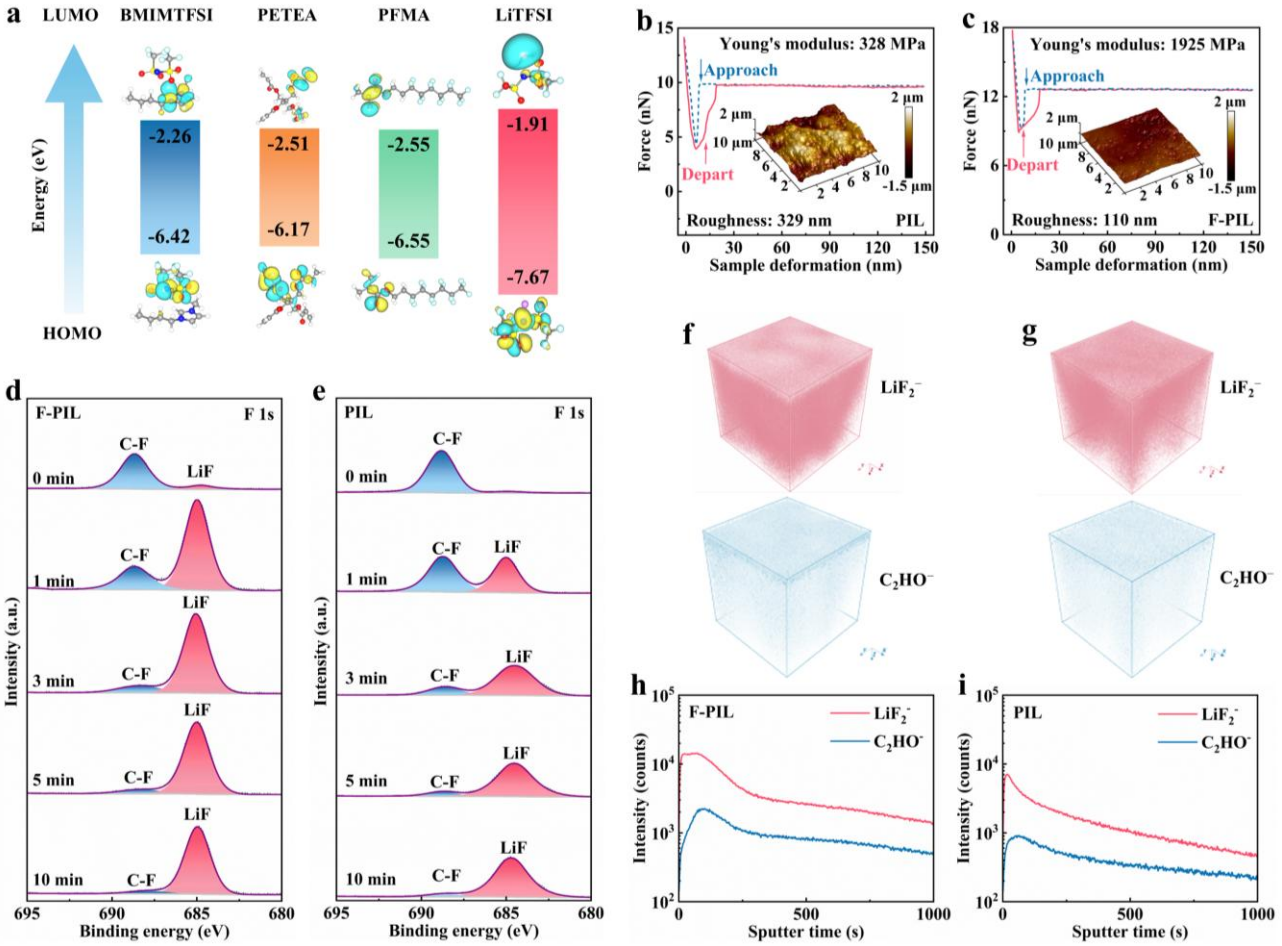

Figure 6. Morphological and compositional analysis of two interphases. (a) HOMO and LUMO energy levels of BmimTFSI, PETEA, PFMA and LiTFSI. Force-displacement plots of (b) PIL derived CEI and (c) F-PIL derived CEI. Corresponding three-dimensional AFM scanning images of CEI layers are shown in insets. In-depth XPS spectra for the (d) F-PIL and (e) PIL after cycling. 3D views of LiF_2^- and C_2HO^- distributions in the SEI that formed in Li||LFP cells with the (f) F-PIL and (g) PIL. TOF-SIMS depth profiling of secondary ion fragments on the SEI using (h) F-PIL and (i) PIL.

Depth-etching XPS and time-of-flight secondary ion mass spectrometry (TOF-SIMS) were employed to analyze the SEI composition on cycled lithium anodes. Figure 6d presents the F 1s spectra of the SEI in F-PIL. The surface of the SEI is predominantly composed of C-containing organic components (C−F) and inorganic components (LiF), primarily derived from the decomposition of PFMA decomposition and subsequent F^- ion interaction with Li^+. As the sputtering depth increases, the organic signal diminishes, and LiF becomes the dominant component throughout the depth profile. In contrast, the SEI in PIL exhibits significantly lower LiF amounts (Figure 6e). TOF-SIMS measurements were adopted to observe the distribution of different components in the SEI, including LiF_2^- and C_2HO^-. The 3D view (Figures 6f and 6g) and high-intensity spectra (Figures 6h

and 6i) indicate that the SEI components are primarily located in the outer layer, with the LiF_2^- peak in F-PIL being notably stronger than in PIL.[24]

2.6 Electrochemical performance of full cells and kinetic analysis

To evaluate the effectiveness of the F-PIL electrolyte in enhancing electrode stability and reversibility, quasi-solid-state Li||LFP cells were assembled using both F-PIL and PIL electrolytes. The coin cells underwent two initial cycles at 0.1 C, followed by cycles at 1 C within a voltage range of 2.5-3.8 V. As presented in **Figure 7**a, the discharge capacity of the Li|PIL|LFP cell significantly decreases after 100 cycles, while the Li|F-PIL|LFP cell maintains 80% of its initial capacity over 600 cycles. Furthermore, the average CE of the F-PIL electrolyte during cycling reached 99.27%, notably higher than the 98.49% observed for PIL (Figure S18). As illustrated in Figures S19 and S20, the capacity-voltage profiles indicate that the capacity decay of the Li|F-PIL|LFP cell is significantly smaller within 120 cycles compared to that of the Li|PIL|LFP cell, suggesting enhanced interface stabilization and kinetic processes. Moreover, the Li|F-PIL|LFP cell demonstrates excellent rate performance. At rates of 0.5, 1, 1.5, and 2 C, the cells deliver capacities of 157.5, 149.3, 142.6, and 136.5 mAh g^{-1}, respectively. When cycled back to 0.5 C, the cell retains a high capacity of 156.6 mAh g^{-1}, which is significantly better than the PIL system (initial/final 0.5C capacity: 156.0/146.8 mAh g^{-1}) (Figure 7b). Additionally, the cycling performance of NCM811 cathodes paired with PIL and F-PIL electrolytes was tested at 0.5 C (2.8-4.3 V). As shown in Figure 7c, the Li|PIL|NCM811 cell retains only 80% capacity after 84 cycles, while the Li|F-PIL|NCM811 cell maintains 80% capacity over 240 cycles – a threefold improvement in cycle life. As illustrated in Figures S21 and S22, the capacity-voltage profiles indicate that the capacity decay of the Li|F-PIL|NCM811 cell is significantly smaller within 240 cycles compared to that of the Li|PIL|LFP cell. Figure 7d displays the rate capabilities of the NCM811 cathode. When the current density increases from 0.5 C to 2 C, the capacity of cathode of the Li|PIL|NCM811 cells decreases rapidly. In contrast, the capacity of the Li|F-PIL|NCM811 decreases slowly, indicating its superior rate performance. To further understand the reversibility of

the cathode structure and the enhancement of Li^+ migration kinetics during cycling, CV curves were plotted for both F-PIL and PIL. The CV curves of PIL exhibits poor overlap of redox peaks due to inhomogeneous phase transition during cycling. In contrast, the CV curves of F-PIL shows well-defined, overlapping peaks, indicating highly reversible electrochemical reaction in the Li|F-PIL|LFP system (Figure S23).

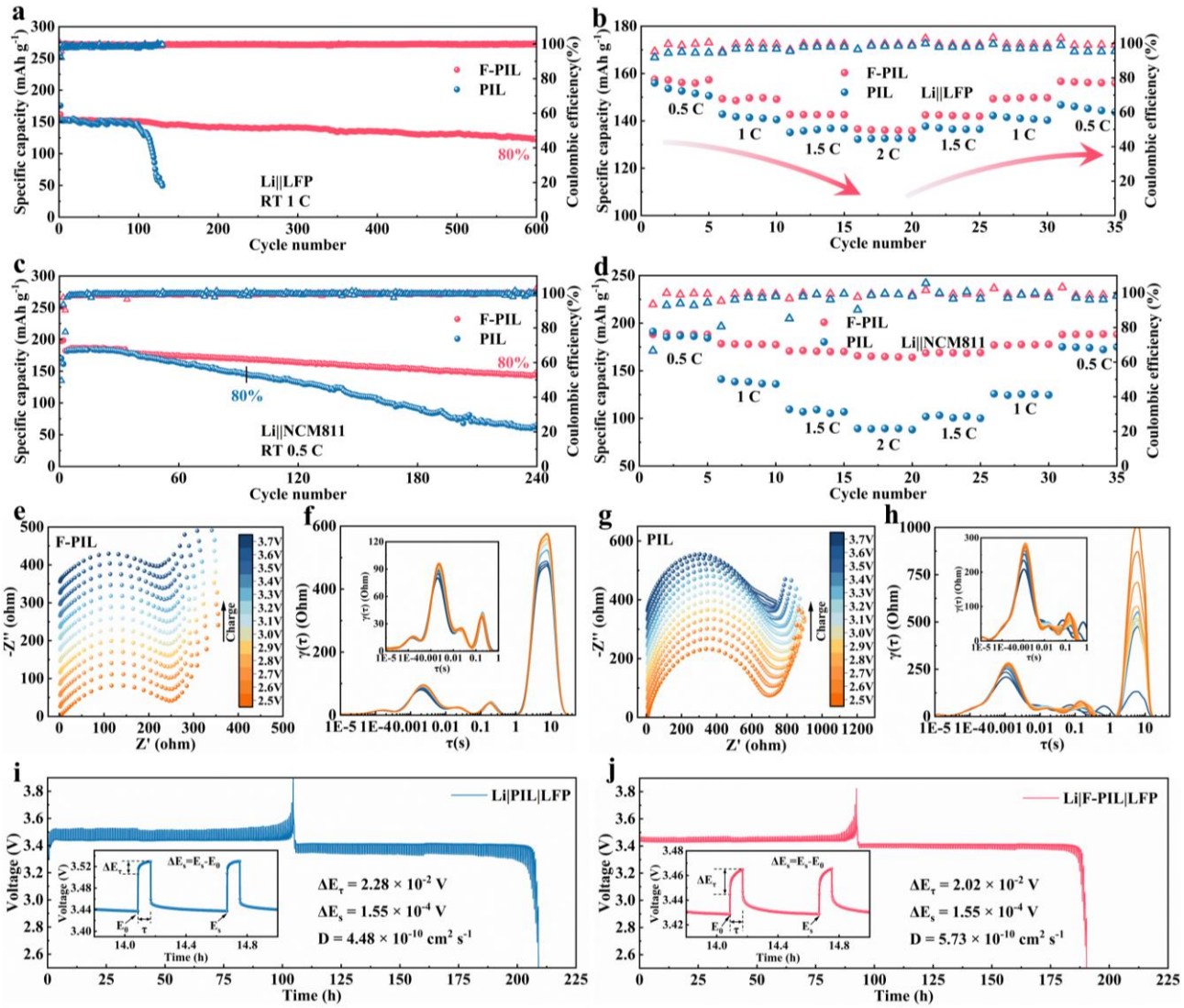

Figure 7. Electrochemical performance of full cells and kinetic analysis. (a) Cycling performance of Li||LFP cells at 2.5~3.8 V using F-PIL and PIL. (b) Rate capacities of Li||LFP cells using F-PIL and PIL. (c) Cycling performance of Li||NCM811 cells at 2.8~4.3 V using F-PIL and PIL. (d) Rate capacities of Li||NCM811 cells using F-PIL and PIL. Nyquist plots obtained from IS-GEIS results of (e) F-PIL and (g) PIL cells at 0.5 C with an equidistant voltage of 0.1 V during charging process and corresponding DRT transformation of IS-GEIS results of (f) F-PIL and (h) PIL during charging process. GITT profiles of the (i) PIL and (j) F-PIL.

To investigate the impedance evolution in the Li|F-PIL|LFP cell, *in-situ* galvanostatic electrochemical impedance spectra (IS-GEIS) were conducted at a constant voltage of 0.1 V. The Nyquist plots (Figures 7e and S24a) reveal no significant increase in interfacial impedance or phase

change during cycling, indicating stable operation of the Li|F-PIL|LFP cell. In contrast, significant impedance changes are observed in the Li|PIL|LFP cell (Figures 7g and S25a). The impedance spectra were further analyzed using the distribution of relaxation times (DRT) technique, decomposing the total impedance into five components: ohmic impedance (R_0), SEI impedance (R_{SEI}), cathode interfacial charge transfer impedance (R_{ct1}), anode interfacial charge transfer impedance (R_{ct2}), and Warburg impedance (R_w). As shown in Figures 7f and S24b, the Li|F-PIL|LFP cell exhibits very low resistance values across all components, with minimal variation during cycling. The R_{ct} values show excellent reversibility, confirming the stable operation of F-PIL during battery cycling. In contrast, the IS-GEIS results for the Li|PIL|LFP cell (Figures 7h and S25b) demonstrates significantly higher and more variable R_{ct} values during cycling, consistent with the previous analysis that PIL does not provide sufficient electrochemical performance for long-term stability.[25]

Galvanostatic intermittent titration technique (GITT) measurements were conducted to probe Li^+ transport characteristics, employing 0.5 C pulse currents with 8 min polarization/30 min relaxation intervals. As shown in Figures 7i and 7j, the voltage plateaus for Li|F-PIL|LFP is lower than that for Li|PIL|LFP, indicative of mitigated electrochemical polarization. Li^+ diffusion coefficients for the electrodes were calculated from the GITT curves, with values of 4.48×10^{-10} cm^2 s^{-1} for Li|PIL|LFP and 5.73×10^{-10} cm^2 s^{-1} for Li|F-PIL|LFP. These results confirm that F-PIL not only reduces charge-transfer resistance but also facilitates Li^+ diffusion, contributing to enhanced cycling stability and rate capability of batteries.

3. Conclusion

In conclusion, the proposed triadic molecular synergy strategy effectively integrates the advantages of polymer-salt, ionic liquids, and fluorinated copolymer additives to decouple lithium-ion conduction in flame-retardant quasi-solid electrolytes. Among these components, the LiTFSI-PETEA cross-linked network provides mechanical support, the BmimTFSI ionic liquid performs both plasticizer and flame-retardant functions, while the PFMA fluorinated copolymer achieves a synergistic effect based

on the Li^+ dissociation promotion and anion anchoring through electronic structural regulation. As a result, the developed F-PIL electrolyte exhibits decent ionic conductivity (1.84×10^{-3} S cm^{-1}) and a high Li-ion transference number (0.72) at 25 °C. This strategy leads to exceptional electrochemical performance in Li symmetric cells, Li||$LiFePO_4$ and Li||$LiNi_{0.8}Co_{0.1}Mn_{0.1}O_2$ cells. Additionally, the design enhances battery safety through a condensed-phase flame-retardant mechanism. This work breaks the boundary of electrolyte performance through molecular synergy design and provides a new paradigm for the development of high-safety quasi-solid lithium metal batteries.

4. Experimental

Materials

Pentaerythritol Tetraacrylate (PETEA, ≥80%) stabilized with MEHQ, Lithium bis(trifluoromethanesulphonyl)imide (LiTFSI, ≥99%), 1-Butyl-3-methylimidazolium bis(trifluoromethylsulfonyl)imide (BmimTFSI, ≥98%), 2-(Perfluorohexyl)ethyl methacrylate (PFMA, ≥98%), and 2,2'-Azobis(2-methylpropionitrile) (AIBN, ≥95%) were purchased from Aladdin.

Preparation of F-PIL electrolytes

The F-PIL precursor was formulated through sequential solution processing: First, a 0.5 M LiTFSI/PETEA solution was prepared by dissolving 1.44 g LiTFSI in 10 mL PETEA solvent. This PETEA-salt matrix was then blended with BmimTFSI ionic liquid at 1:1 v/v ratio under magnetic stirring (25°C, 6 h). Subsequently, 2 mL PFMA was introduced into the mixture (BmimTFSI: PFMA = 5:1 v/v) followed by additional homogenization (25°C, 6 h). The polymerization process was initiated by adding 1 wt% AIBN thermal initiator, with subsequent 30-min stirring ensuring precursor homogeneity prior to *in-situ* thermal polymerization. Finally, 30 μl of the precursor solution was poured into the mold and placed in an oven at 70°C for 2 hours. The non-fluorinated PIL electrolyte was synthesized analogously to F-PIL, omitting PFMA addition. The identical PETEA-salt/BmimTFSI (1:1 v/v) matrix underwent AIBN-initiated polymerization under equivalent thermal and temporal conditions.

Characterization

SEM (ZEISS Sigma 300) was used to observe the morphology of the F-PIL membrane and the elemental distribution. XRD (Rigaku SmartLab SE) was performed to analyze the crystal structure of the samples. FTIR spectra were obtained using a Thermo Fisher Scientific Nicolet iS5 spectrometer. Raman spectra were employed for group analysis of the two electrolytes (Thermo Scientific DXR and Renishaw inVia Plus). The heat release and smoke release properties were evaluated using a cone calorimeter. Thermal stability was evaluated through TG-FTIR (Thermo Fisher IS5, NETZSCH 209F1) in a nitrogen atmosphere at a heating rate of 10 °C min^{-1}. *In-situ* optical imaging was conducted using a Zeiss Smartzoom 5. ^{7}Li NMR spectroscopy were performed on Bruker Avance NEO 600 NMR spectrometers. DSC were measured using the HITACHI STA200 Synchronous thermal analyzer under N_2 flow with a heating rate of 10 °C min^{-1}. The stress-strain curves are performed on a universal test machine. The bruker DimensonICON was used to measure the Young's modulus, roughness and surface morphology. The SEI component and 3D distribution were collected by TOF-SIMS (PHI nanoTOF II, 30 keV, 2 nA).

Electrochemical measurements

The cathodes were prepared by mixing commercial LFP (or NCM811) powder with PVDF and Super P (weight ratio of 8:1:1) in NMP solvent. The obtained slurry was coated onto carbon-coated aluminum foil and then dried at 80 °C for 12 hours. Load was controlled by 2.7 ~ 2.8 mg. Symmetrical coin-type cells and asymmetric full cells were assembled using Celgard 2400 separator in an argon-filled glove box (H_2O and $O_2 \leq 0.1$ ppm). Electrochemical tests were performed using electrochemical workstation (CHI660E, Bio-Logic VMP3) and battery test system (Wuhan LAND Electronics Co., Ltd.).

CRediT authorship contribution statement

Kun Li: Conceptualization, Visualization, Methodology, Writing – original draft. **Anjun Hu**: Investigation, Writing-review & editing. **Ruizhe Xu:** Conceptualization, Visualization. **Wang Xu:** Conceptualization, Visualization. **Borui Yang:** Conceptualization, Visualization. **Ting Li:** Formal

analysis, Validation. **Yuanjian Li:** Investigation, Writing – review & editing. **Zhi Wei Seh:** Formal analysis, Validation. **Jianping Long:** Writing – review & editing, Funding acquisition, Project administration, Supervision. **Shimou Chen:** Investigation, Writing – review & editing.

Supporting Information

Supporting Information is available from the Wiley Online Library or from the author.

Acknowledgements

This work was supported by the Lithium Resources and Lithium Materials Key Laboratory of Sichuan Province (LRMKF202405), the National Natural Science Foundation of China (52402226), the Natural Science Foundation of Sichuan Province (2024NSFSC1016), and the Scientific Research Startup Foundation of Chengdu University of Technology (10912-KYQD2023-10240), the Singapore National Research Foundation (NRF Investigatorship NRF-NRFI09-0002), and the Agency for Science, Technology and Research (MTC Programmatic Fund M23L9b0052).

Conflict of Interest

The authors declare no conflict of interest.

Data Availability Statement

The data that support the findings of this study are available from the corresponding author upon reasonable request.

References

[1] a) S. Chen, G. Wu, H. Jiang, J. Wang, T. Chen, C. Han, W. Wang, R. Yang, J. Zhao, Z. Tang, External Li supply reshapes Li deficiency and lifetime limit of batteries, *Nature* 2025, 638, 676; b) X. Hu, Z. Zhang, X. Zhang, Y. Wang, X. Yang, X. Wang, M. Fayena-Greenstein, H. A. Yehezkel, S. Langford, D. Zhou, External-pressure–electrochemistry coupling in solid-state lithium metal batteries, *Nat. Rev. Mater.* 2024, 9, 305; c) H. Song, K. Münch, X. Liu, K. Shen, R. Zhang, T. Weintraut, Y. Yusim, D. Jiang, X. Hong, J. Meng, All-solid-state Li–S batteries with fast solid–solid sulfur reaction, *Nature* 2025, 637, 846.

[2] a) D. Lu, R. Li, M. M. Rahman, P. Yu, L. Lv, S. Yang, Y. Huang, C. Sun, S. Zhang, H. Zhang, Ligand-channel-enabled ultrafast Li-ion conduction, *Nature* 2024, 627, 101; b) A. Hu, W. Chen, F. Li, M. He, D. Chen, Y. Li, J. Zhu, Y. Yan, J. Long, Y. Hu, Nonflammable polyfluorides-anchored quasi-solid electrolytes for ultra-safe anode-free lithium pouch cells without thermal runaway, *Adv. Mater.* 2023, 35, 2304762; c) A. Hu, F. Li, W. Chen, T. Lei, Y. Li, Y. Fan, M. He, F. Wang, M. Zhou, Y. Hu, Ion Transport Kinetics in Low-Temperature Lithium Metal Batteries, *Adv. Energy Mater.* 2022, 12, 2202432; d) S. J. Yang, J. K. Hu, F. N. Jiang, H. Yuan, H. S. Park, J. Q. Huang, Safer solid-state lithium metal batteries: Mechanisms

and strategies, *InfoMat* 2024, 6, e12512.

[3] a) X. Lu, Y. Wang, X. Xu, B. Yan, T. Wu, L. Lu, Polymer-Based Solid-State Electrolytes for High-Energy-Density Lithium-Ion Batteries–Review, *Adv. Energy Mater.* 2023, 13, 2301746; b) S. Huo, L. Sheng, W. Xue, L. Wang, H. Xu, H. Zhang, X. He, Challenges of polymer electrolyte with wide electrochemical window for high energy solid-state lithium batteries, *InfoMat* 2023, 5, e12394; c) W. Ma, X. Cui, Y. Chen, S. Wan, S. Zhao, J. Gong, G. Wang, S. Chen, Designing a Refined Multi-Structural Polymer Electrolyte Framework for Highly Stable Lithium-Metal Batteries, *Angew. Chem. Int. Ed.* 2025, 137, e202415617.

[4] L.-Z. Fan, H. He, C.-W. Nan, Tailoring inorganic–polymer composites for the mass production of solid-state batteries, *Nat. Rev. Mater.* 2021, 6, 1003.

[5] a) H. An, M. Li, Q. Liu, Y. Song, J. Liu, Z. Yu, X. Liu, B. Deng, J. Wang, Strong Lewis-acid coordinated PEO electrolyte achieves 4.8 V-class all-solid-state batteries over 580 Wh kg^{-1}, *Nat. Commun.* 2024, 15, 9150; b) C.-D. Fang, Y. Huang, Y.-F. Sun, P.-F. Sun, K. Li, S.-Y. Yao, M.-Y. Zhang, W.-H. Fang, J.-J. Chen, Revealing and reconstructing the 3D Li-ion transportation network for superionic poly (ethylene) oxide conductor, *Nat. Commun.* 2024, 15, 6781; c) S. Wan, W. Ma, Y. Wang, Y. Xiao, S. Chen, Electrolytes design for extending the temperature adaptability of lithium-ion batteries: from fundamentals to strategies, *Adv. Mater.* 2024, 36, 2311912.

[6] a) Z. Wang, C. Su, R. Xu, K. Li, B. Yang, T. Li, K. Chen, W. Xu, J. Chen, F. Li, Weak traction effect modulates anionic solvation transition for stable-cycling and fast-charging lithium metal batteries, *Energy Storage Mater.* 2025, 75, 104105; b) R. Xu, A. Hu, Z. Wang, K. Chen, J. Chen, W. Xu, G. Wu, F. Li, J. Wang, J. Long, Tailoring anion-dominant solvation environment by steric-hindrance effect and competitive coordination for fast charging and stable cycling lithium metal batteries, *J. Energy Chem.* 2025, 105, 35. c) Z. Chen, W. Zhou, S. Zhao, X. Lou, S. Chen, In-Situ Construction of Solid Electrolyte Interphases with Gradient Zincophilicity for Wide Temperature Zinc Ion Batteries, *Adv. Energy Mater.*, 2024, 14, 2404108.

[7] H. Xu, J. Yang, Y. Niu, X. Hou, Z. Sun, C. Jiang, Y. Xiao, C. He, S. Yang, B. Li, Deciphering and Integrating Functionalized Side Chains for High Ion-Conductive Elastic Ternary Copolymer Solid-State Electrolytes for Safe Lithium Metal Batteries, *Angew. Chem. Int. Ed.* 2024, 136, e202406637.

[8] Z. Ouyang, Y. Wang, S. Wang, S. Geng, X. Zhao, X. Zhang, Q. Xu, B. Yuan, S. Tang, J. Li, Programmable DNA Interphase Layers for High-Performance Anode-Free Lithium Metal Batteries, *Adv. Mater.* 2024, 36, 2401114.

[9] a) X. Jiang, Z. Liu, W. Liu, D. Yu, J. Zhang, X. Wang, Y. Zhang, S. Zhang, Physical ionogels with only 2 wt% gelators as efficient quasi-solid-state electrolytes for lithium batteries, *Matter* 2024, 7, 1558; b) Z. Liu, Q. Yu, N. Oli, J. F. F. Gomez, S. Qiu, H. Tian, Q. Qiu, W. Sun, K. Li, Z. Liu, A Non-Volatile, Thermo-Reversible, and Self-Protective Gel Electrolyte Providing Highly Precise and Reversible Thermal Protection for Lithium Batteries, *Adv. Energy Mater.* 2023, 13, 2300143.

[10] a) X. Liu, A. Mariani, T. Diemant, M. E. Di Pietro, X. Dong, A. Mele, S. Passerini, Reinforcing the Electrode/Electrolyte Interphases of Lithium Metal Batteries Employing Locally Concentrated Ionic Liquid Electrolytes, *Adv. Mater.* 2024, 36, 2309062; b) S. Zhang, S. Wu, J. Hwang, K. Matsumoto, R. Hagiwara, Unprotected Organic Cations─The Dilemma of Highly Li-Concentrated Ionic Liquid Electrolytes, *J. Am. Chem. Soc.* 2024, 146, 8352.

[11] S. Li, H. Hong, D. Li, X. Yang, S. Wang, D. Zhang, Q. Xiong, Z. Huang, C. Zhi, Designing Zwitterionic Bottlebrush Polymers to Enable Long-Cycling Quasi-Solid-State Lithium Metal Batteries, *Angew. Chem. Int. Ed.* 2025, 64, e202409500.

[12] S. Wang, S. Xiao, S. Li, C. Liu, H. Cai, W. Sun, Z. D. Huang, W. Y. Lai, Organic Cationic-Coordinated Perfluoropolymer Electrolytes with Strong Li^+-Solvent Interaction for Solid State Li-Metal Batteries, *Angew. Chem. Int. Ed.* 2024, 63, e202412434.

[13] F. Hai, Y. Yi, Z. Xiao, J. Guo, X. Gao, W. Chen, W. Xue, W. Hua, W. Tang, M. Li, A Low-Cost, Fluorine-Free Localized Highly Concentrated Electrolyte Toward Ultra-High Loading Lithium Metal Batteries, *Adv. Energy Mater.* 2024, 14, 2304253.

[14] Z. Li, S. Zhu, S. Gao, Y. He, H. Ding, D. Yang, H. Yang, P. F. Cao, Fireproof Solid Polymer Electrolyte with Chemically Bonded Phosphorus Toward Stable and Safe Lithium-Metal Battery, *Adv. Funct. Mater.* 2024, 34, 2409836.

[15] a) X. Song, Z.-P. Deng, C.-B. Li, F. Song, X.-L. Wang, L. Chen, D.-M. Guo, Y.-Z. Wang, A bio-based epoxy resin derived from p-hydroxycinnamic acid with high mechanical properties and flame retardancy, *Chin. Chem. Lett.* 2022, 33, 4912; b) L. Han, C. Liao, Y. Liu, H. Yu, S. Zhang, Y. Zhu, Z. Li, X. Li, Y. Kan, Y. Hu, Non-flammable sandwich-structured TPU gel polymer electrolyte without flame retardant addition for high performance lithium ion batteries *Energy Storage Mater.* 2022, 52, 562.

[16] B. Yang, Y. Pan, T. Li, A. Hu, K. Li, B. Li, L. Yang, J. Long, High-safety lithium metal pouch cells for extreme abuse conditions by implementing flame-retardant perfluorinated gel polymer electrolytes, *Energy Storage Mater.* 2024, 65, 103124.

[17] Y. Lu, Y. Zhang, K. Zhang, Renewable biomass resources to access halogen-and phosphorus-free flame retardant thermosets with ultra-low heat release capacity, *Chem. Eng. J.* 2022, 448, 137670.

[18] a) Y. F. Huang, J. P. Zeng, S. F. Li, C. Dai, J. F. Liu, C. Liu, Y. B. He, Conformational Regulation of Dielectric Poly (Vinylidene Fluoride)-Based Solid-State Electrolytes for Efficient Lithium Salt Dissociation and Lithium-Ion Transportation, *Adv. Energy Mater.* 2023, 13, 2203888; b) H. Y. Zhou, Y. Ou, S. S. Yan, J. Xie, P. Zhou, L. Wan, Z. A. Xu, F. X. Liu, W. L. Zhang, Y. C. Xia, Supramolecular Polymer Ion Conductor with Weakened Li Ion Solvation Enables Room Temperature All-Solid-State Lithium Metal Batteries, *Angew. Chem. Int. Ed.* 2023, 135, e202306948.

[19] T. Wang, B. Chen, C. Liu, T. Li, X. Liu, Build a High-Performance All-Solid-State Lithium Battery through Introducing Competitive Coordination Induction Effect in Polymer-Based Electrolyte, *Angew. Chem. Int. Ed.* 2024, 63, e202400960.

[20] Y. Ma, Y. Qiu, K. Yang, S. Lv, Y. Li, X. An, G. Xiao, Z. Han, Y. Ma, L. Chen, Competitive Li-ion coordination for constructing a three-dimensional transport network to achieve ultra-high ionic conductivity of a composite solid-state electrolyte, *Energy Environ. Sci.* 2024, 17, 8274.

[21] a) M. Cui, Y. Qin, Z. Li, H. Zhao, L. Liu, Z. Jiang, Z. Cao, J. Zhao, B. Mao, W. Yu, Retarding anion migration for alleviating concentration polarization towards stable polymer lithium-metal batteries, *Sci. Bull.* 2024, 69, 1706; b) X. M. Lu, H. Wang, Y. Sun, Y. Xu, W. Sun, Y. Wu, Y. Zhang, C. Yang, Y. Wang, Covalent Triazine Based Frameworks with Donor-Donor-π-Acceptor Structures for Dendrite-Free Lithium Metal Batteries, *Angew. Chem. Int. Ed.* 2024, 136, e202409436.

[22] S. Gu, Y. Zhang, M. Li, G. Xu, N. Zhang, Internal Electron-Donation Allocation Design for Intrinsic Solubilization of Lithium Nitrate in Ester Electrolyte for Stable Lithium Metal Batteries, *Angew. Chem. Int. Ed.* 2024, 64, e202410020.

[23] Y. Liu, Z. Jin, Z. Liu, H. Xu, F. Sun, X. Q. Zhang, T. Chen, C. Wang, Regulating the Solvation Structure in Polymer Electrolytes for High-Voltage Lithium Metal Batteries, *Angew. Chem. Int. Ed.* 2024, 136, e202405802.

[24] a) Y. Gao, Z. Wang, H. Tu, J. Xue, S. Weng, S. Lu, L. Liu, G. Sun, K. Peng, X. Zhang, Low-Temperature and Fast-Charging Sodium Metal Batteries Enabled by Molecular Structure Regulation of Fluorinated Solvents, *Adv. Funct. Mater.* 2024, 35, 2414652; b) A. Hu, W. Chen, X. Du, Y. Hu, T. Lei, H. Wang, L. Xue, Y. Li, H. Sun, Y. Yan, An artificial hybrid interphase for an ultrahigh-rate and practical lithium metal anode, *Energy Environ. Sci.* 2021, 14, 4115.

[25] a) J. Zhang, C. Zheng, L. Li, Y. Xia, H. Huang, Y. Gan, C. Liang, X. He, X. Tao, W. Zhang, Unraveling the intra and intercycle interfacial evolution of Li_6PS_5Cl-based all-solid-state

lithium batteries ‚*Adv. Energy Mater.* 2020, 10, 1903311; b) T. Yang, W. Zhang, Y. Liu, J. Zheng, Y. Xia, X. Tao, Y. Wang, X. Xia, H. Huang, Y. Gan, High-Performance Solid Lithium Metal Batteries Enabled by LiF/LiCl/LiIn Hybrid SEI via $InCl_3$-Driven In Situ Polymerization of 1, 3-Dioxolane, *Small* 2023, 19, 2303210.

In this study, we propose a molecular-level triadic molecular synergy paradigm that integrates a polymer-salt matrix, an ionic liquid dynamic plasticizer, and a fluorinated copolymer additive to overcome the longstanding challenge of synergizing ion transport, interfacial stability, and intrinsic safety in quasi-solid polymer electrolytes for high-performance lithium metal batteries.

Keywords: Lithium-metal batteries; Quasi-solid electrolytes; Ionic liquids; Ion Transport; Flame retardancy

Kun Li, Anjun Hu, Ruizhe Xu, Wang Xu, Borui Yang, Ting Li, Yuanjian Li, Zhi Wei Seh, Jianping Long, Shimou Chen

Decoupled Ion Transport via Triadic Molecular Synergy in Flame-Retardant Quasi-Solid Electrolytes for Safe Lithium-Metal Batteries